Foot-Mounted Inertial Navigation - Implementation and Fusion Concept into a Bayesian Filtering Framework

Karin Mascher[1], Manfred Wieser[1]

[1]*Institute of Geodesy, Graz University of Technology, Steyrergasse 30, 8010 Graz, Austria*

Abstract
A reliable underground navigation system for task forces in emergency scenarios increases safety and effectiveness. Since smoke, explosions or disturbed power supply complicate the operations below ground, the correct visualization of the task forces' positions has become a key element in obtaining a successful outcome. A foot-mounted inertial navigation system provides an autonomous way to navigate in Global Navigation Satellite Systems (GNSS)-denied environments. The additional use of maps and absolute positioning methods (Wi-Fi Round Trip Time (RTT), Ultra-Wideband (UWB), ...) represent one way to build a robust navigation system for emergency operations underground. This study proposes a sensor fusion concept to combine a foot-mounted inertial navigation system (INS) with distance measurements and map information. However, the main emphasis in this paper is on the implementation of a foot-mounted INS. Therefore, a Zero-Velocity-Aided Error-State (Extended) Kalman Filter is utilized. The filter is based on the mechanization equation that expresses the position in the earth-fixed frame, the velocity in the local-level frame and the attitude in the body frame. The performance analysis of the foot-mounted INS as a single system showed that a stable position solution over several hundred meters could be achieved.

Keywords
Inertial Navigation, Pedestrian Navigation System, IMU, Underground Navigation, Sensor Fusion

1. Introduction

A reliable navigation system (accurate and robust) is an important safety requirement for emergency response personnel and forces. Underground navigation, such as in tunnels, represents a big challenge since Global Navigation Satellite Systems (GNSS) do not offer enough signal quality to obtain a positioning solution. Furthermore, in emergencies/disasters, the underground environment can be dominated by no/poor lighting or smoke. Such environmental conditions can endanger the success of the rescue operation. Accurate positioning of the emergency/military team would increase the safety of everyone involved and concerned. Real-time visualization of positions would also facilitate the operational control management for the command post and make it more effective [1, 2]. The key to a reliable navigation system is the choice of the appropriate sensors.

1.1. State-Of-The-Art

One possible sensor is an Inertial Measurement Unit (IMU). An IMU is a common sensor for autonomous positioning techniques [3] and is well suited for indoor positioning purposes. However, IMUs show drift behaviors. The position solution drifts away from the correct one as time passes [4]. One way to bound the drift is to introduce Zero-Velocity Updates (ZUPT) during standstill periods. An IMU mounted on the foot of a human being, for example, enables such utilization in the form of a Zero-Velocity-Aided Inertial Navigation System (INS) (cf. Open-Shoe [5]). A Zero-Velocity-Aided INS offers the correct processing of complex movements, such as backward/lateral walks or crawling, which are conventional movements of task forces. In addition to the ZUPTs, dual foot-mounted IMUs (one IMU on each foot) can help to mitigate symmetrical modeling errors, such as the systematic heading drift [6, 4].

The fusion of multiple sensors makes a navigation system more robust and reliable. Studies from [7, 8], for example, used dual foot-mounted inertial sensors and Ultra-Wideband (UWB) ranging devices for robust cooperative localization. Yang et al. [9] proposed a particle-filter-based prediction approach to fuse a dual foot-mounted INS with map information. The authors of [10] developed a tightly coupled indoor positioning system based on pedestrian dead reckoning and Wi-Fi Round Trip Time (RTT). All studies showed promising results.

1.2. Sensor Fusion Concept

In this project, an INS, distance measuring techniques (Wi-Fi RTT or UWB) and map information are fused to obtain a reliable underground navigation system for task forces in GNSS-denied environments. A possible concept for an underground navigation system is illustrated in Figure 1. The basic idea is to integrate the foot-mounted IMUs into a Bayesian filtering framework [11]. Thus, a dual foot-mounted INS will be developed that provides a robust estimation of, among others, (step-wise) position changes. The use of IMUs on both feet can significantly reduce the systematic heading drift as proposed in [4, 12]. The INS will be realized as a conventional strap-down combined with a Zero-Velocity-Aided Error-State (Extended) Kalman Filter (EKF). The EKF standard approach is chosen since it is computationally inexpensive and shows a relatively low complexity in contrast to, for example, a particle filter. Since the IMUs generally operate at a relatively high sampling rate, the estimated position changes are integrated step-wise to the particle filter, where the main sensor fusion takes place at a lower sampling rate.

The particle filter provides an easy integration of nonlinear observations such as map information (probability maps) [11]. Maps of tunnel structures are used as artificial sensors. For instance, the lateral position error can be bounded by the tunnel cross-section. The absolute position information is derived from distance measurements (Wi-Fi RTT or UWB) to known anchors. In case that at least three distance measurements are available, trilateration delivers an absolute position. If not, the distance measurements are used to re-weight the particles [13]. The position estimates of the task forces will be visualized in a virtual reality environment.

1.3. Novelty

The use of absolute positioning methods require a preinstalled infrastructure. However, during emergency scenarios below ground such infrastructure is not available or, even if they are, they
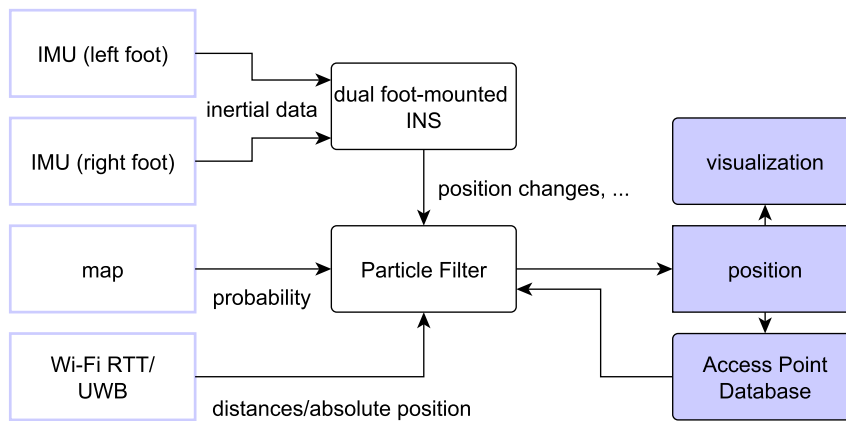
Figure 1: Preliminary system architecture for the positioning system.

could be damaged. The idea in this project is to built the needed infrastructure during operating time, in other words, to install dynamically the Wi-Fi/UWB access points. The approximate coordinates of the access points are derived from the INS and the map information and stored in the corresponding database (Figure 1). Once the access points are installed, all available sensors (IMU, Wi-Fi RTT/UWB, map) are fused to obtain the task force's positions and also to update the positions of the access points. The determination of the start position is still an open topic.

However, the main focus is put on the implementation and performance analysis of a "single" foot-mounted INS. In future studies, an approach to fuse the data of a dual foot-mounted INS will be developed as well as the concrete integration into the particle filter.
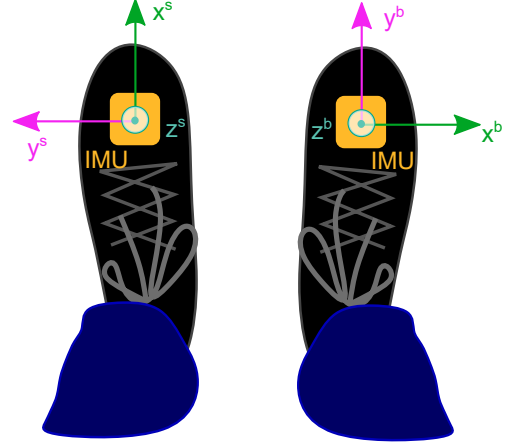
2. Test Setup

For the foot-mounted PDR system, the XSens Dot [14], produced by *XSens*, is utilized as IMU. The XSens Dot is composed of triaxial micro-electro-mechanical systems (MEMS) accelerometers, triaxial MEMS gyroscopes and triaxial MEMS magnetometers. It is a wearable sensor and features wireless data transmission based on Bluetooth 5.0. The acceleration and angular data are sensed internally at a high-frequency rate (800 Hz). Due to limitations of the Bluetooth's channel bandwidth, the data is finally provided in real-time at 60 Hz using an intern strap-down integration by XSens [14]. The data is recorded using a smartphone and the "Xsens Dot" App, which is available in the App Store as well as in the Play Store. Furthermore, multiple sensors can be time-synchronized with each other [14]. For the test setup, two IMUs are mounted onto the left and the right foot, respectively, as seen in Figure 2a.

3. Coordinate Systems

The raw measurements (accelerations, angular rates, magnetic field strength) refer to the sensor frame (s-frame). The s-frame on Xsens Dot [14] is displayed in Figure 2b. The body frame

(a) Test Setup.

(b) Sensor Orientation. The sensor frame and body frame are indicated by the superscripts s and b, respectively.

Figure 2: Test Setup and Sensor Orientation.

(b-frame) here is defined so that the y-axis points in the forward direction, the x-axis to the right and the z-axis is orthogonal to them and points upwards [15]. Thus, a right-handed system is completed (Figure 2b). The local-level frame (l-frame) is expressed in terms of east north up (ENU). The Earth-Centered Earth-Fixed Frame (ECEF) is denoted as e-frame. The WGS 84 ellipsoid is used [16].

4. IMU-Signal Processing

The sensors are calibrated according to [17]. The IMU calibration was done just for investigation purposes, whether the in-factory calibration is satisfactory or not. To get an first impression, the focus was put on biases only. The highest obtained biases were 0.12 m/s^2 and 0.45 °/s for the accelerometer and gyroscope, respectively. However, since the gyroscope biases can vary strongly between different measurement sets, it is recommended to estimate them from stationary phases during each set [17]. The magnetometer is calibrated using the Magnetic Field Mapper provided by XSens. Furthermore, the measurements need to be transformed from the s-frame into the b-frame. This is accomplished by performing a simple 90-degree rotation around the z-axis ($z = z^b = z^s$) (cf. Figure 2b).

The following subsection presents the used approach for the foot-mounted Zero-Velocity-Aided INS. The measured accelerations (specific forces) and the measured angular rates are denoted as f^b and ω_{ib}^b, respectively. Both refer to the b-frame.

4.1. INS Mechanization

The used mechanization equation is expressed as a set of three first-order differential equations [3, 15, 18]:

$$
\begin{bmatrix} \dot{\boldsymbol{x}}^e \\ \dot{\mathbf{v}}^l \\ \dot{\mathbf{R}}_b^l \end{bmatrix} = \begin{bmatrix} \mathbf{R}_l^e \mathbf{v}^l \\ \mathbf{R}_b^l \mathbf{f}^b - \left(2\boldsymbol{\Omega}_{ie}^l + \boldsymbol{\Omega}_{el}^l \right) \mathbf{v}^l + \bar{\mathbf{g}}^l \\ \mathbf{R}_b^l \left(\boldsymbol{\Omega}_{ib}^b - \boldsymbol{\Omega}_{il}^b \right) \end{bmatrix}, \tag{1}
$$

where $\mathbf{x}^e$ represents the position in the e-frame in terms of Cartesian coordinates (x^e, y^e, z^e), $\mathbf{v}^l$ is the velocity vector (v_e, v_n, v_u) in the l-frame and $\mathbf{R}_b^l$ is the transformation matrix from the b-frame to the l-frame, respectively. This rotation matrix is described in terms by the attitude parameters roll (r), pitch (p) and yaw (y). The parametrization of the rotation matrix is done using quaternions [15, 19]. $\mathbf{R}_l^e$ describes the transformation from the l-frame to the e-frame [3, 15]. Note that the position is expressed in the e-frame, since the visualization tool requires WGS84 coordinates as an input. The (normal) gravity vector in the l-frame is denoted as $\bar{\mathbf{g}}^l = \left[\ 0, 0, \gamma \left(\varphi, h \right) \ \right]^T$. The normal gravity γ depends on the current latitude φ and ellipsoidal height h. The specific force vector $\mathbf{f}^b$ contains the accelerometer measurements. The term $\left(2\boldsymbol{\Omega}_{ie}^l + \boldsymbol{\Omega}_{el}^l \right) \mathbf{v}^l$ refers to the Coriolis part in the measured specific force vector. To be more specific, $\boldsymbol{\Omega}_{ie}^l$ and $\boldsymbol{\Omega}_{el}^l$ are skew-symmetric matrices [15]:

$$
\boldsymbol{\omega}_{ie}^l = \begin{bmatrix} 0 \\ \omega^e \cos \varphi \\ \omega^e \sin \varphi \end{bmatrix} \rightarrow \boldsymbol{\Omega}_{ie}^\ell = \begin{bmatrix} 0 & -\omega^e \sin \varphi & \omega^e \cos \varphi \\ \omega^e \sin \varphi & 0 & 0 \\ -\omega^e \cos \varphi & 0 & 0 \end{bmatrix} \tag{2}
$$

$$
\boldsymbol{\omega}_{el}^l = \begin{bmatrix} -\frac{v_n}{R_M + h} \\ \frac{v_e}{R_N + h} \\ \frac{v_e \tan \varphi}{R_N + h} \end{bmatrix} \rightarrow \boldsymbol{\Omega}_{el}^\ell = \begin{bmatrix} 0 & \frac{-v_e \tan \varphi}{R_N + h} & \frac{v_e}{R_N + h} \\ \frac{v_e \tan \varphi}{R_N + h} & 0 & \frac{v_n}{R_M + h} \\ \frac{-v_e}{R_N + h} & \frac{-v_n}{R_M + h} & 0 \end{bmatrix} \tag{3}
$$

There are dependencies to the geodetic position (φ, h), the current velocity, the Earth's rotation ω^e and the two radii of curvature (R_N and R_M). However, the Coriolis part for a pedestrian is relatively small and could be neglected. Future studies will show whether the consideration of the Coriolis term leads to a noticeable model improvement. The quantity $\boldsymbol{\Omega}_{il}^b$ is composed, according to [15], of:

$$
\boldsymbol{\Omega}_{il}^b = \boldsymbol{\Omega}_{ie}^b + \boldsymbol{\Omega}_{el}^b, \tag{4}
$$

where $\boldsymbol{\Omega}_{ie}^b$ describes the Earth's rotation in the b-frame and $\boldsymbol{\Omega}_{el}^b$ expresses the rate of the orientation change between the e- and l-frame expressed in the b-frame. The term $\boldsymbol{\Omega}_{ib}^b$ is a skew-symmetric matrix containing the gyroscope measurements.

The position, velocity and attitude (PVA) are obtained by integrating Equation 1 over the interval $\Delta t = 1/60$ s. Each estimation of the time epoch t_k is based on the previous PVA solution at t_{k-1} and the currently measured accelerations $\mathbf{f}^b(t_k)$ and angular rates $\boldsymbol{\omega}_{ib}^b(t_k)$. The position/velocity term is obtained by adding the linear integrated velocity/acceleration term to the previous position/velocity solution. The quaternion $\mathbf{q}$ is updated via the closed-form solution shown in [15]. However, more detailed information can be found in [15, 3, 20, 18].
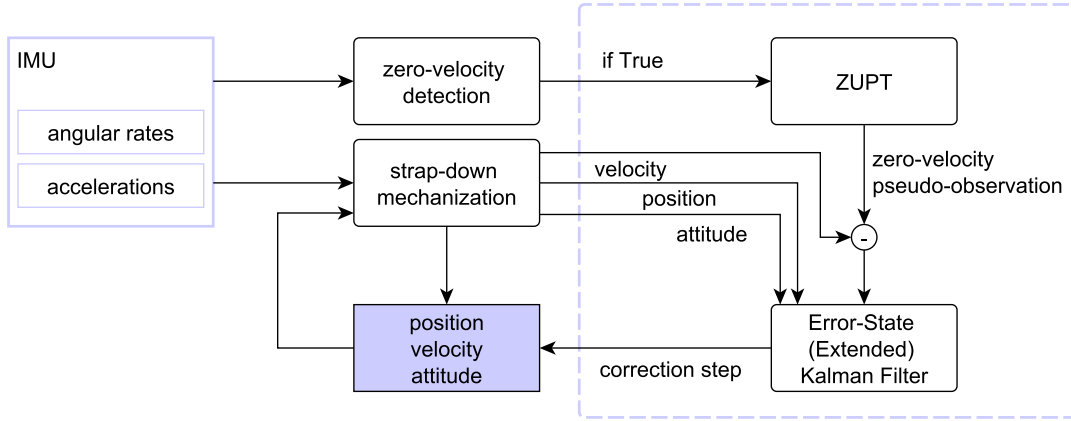
Figure 3: Illustration of Zero-Velocity-Aided INS.

4.2. Zero-Velocity-Aided INS

Equation 1 provides a PVA computation based on the integration of accelerations and angular rates obtained from the IMU and the previous PVA solution. Due to that, sensor errors and measurement noise are accumulated and result in a rapid error growth (drift). However, those effects can be bounded by introducing so-called Zero-Velocity Updates (ZUPT). In this study, the ZUPTs are implemented in form of an Error-State (Extended) Kalman Filter (ESKF). Since the IMUs are mounted onto the shoes, the stance phases of a person are well sensed. During the stance phases, the sensor should output zero velocity. However, this is typically not the case. The zero-velocity is introduced as pseudo-observation in the ESKF [1]. In the case of a zero-velocity event, the estimated velocity from the strap-down algorithm is compared with zero. The estimated error is used to correct the error states. The Zero-Velocity-Aided INS is schematically illustrated in Figure 3.

The system state $\delta\boldsymbol{x}$ consists of the position errors $\delta\boldsymbol{x}^e = [\delta x^e, \delta y^e, \delta z^e]^T$, the velocity errors $\delta\boldsymbol{v}^l = [\delta v_e, \delta v_n, \delta v_u]^T$ and the attitude errors $\delta\boldsymbol{\psi} = [\delta p, \delta r, \delta y]^T$. Sensor errors like biases are not taken into account, since the velocity errors are assumed to be zero-mean, affected by white noise and independent [6]. That typically cannot be fulfilled in a foot-mounted Zero-Velocity-Aided INS [6]. However, the gyroscope error is estimated during prolonged standing. Moreover, it is planned that the final solution includes two foot-mounted IMUs. Using two IMUs have the advantage that symmetrical errors can be eliminated [6] as demonstrated in[4, 12, 9].

The state-space model [15, 4, 20] is shown in Formulas 5 to 7.

$$\delta\dot{\boldsymbol{x}}_{k+1} = \boldsymbol{F}_k\delta\boldsymbol{x}_k + \boldsymbol{G}_k\boldsymbol{w}$$

$$\begin{bmatrix} \delta\dot{\boldsymbol{x}}^e \\ \delta\dot{\boldsymbol{v}}^l \\ \delta\dot{\boldsymbol{\psi}} \end{bmatrix}_{k+1} = \begin{bmatrix} 0 & \boldsymbol{F}_{0,1} & 0 \\ 0 & 0 & \boldsymbol{F}_{1,2} \\ 0 & \boldsymbol{F}_{2,1} & 0 \end{bmatrix}_k \begin{bmatrix} \delta\boldsymbol{x}^e \\ \delta\boldsymbol{v}^l \\ \delta\boldsymbol{\psi} \end{bmatrix}_k + \begin{bmatrix} 0 & 0 \\ \boldsymbol{R}_b^l & 0 \\ 0 & \boldsymbol{R}_b^l \end{bmatrix}_k \boldsymbol{w} \qquad (5)$$

where

$$\boldsymbol{F}_{0,1} = \boldsymbol{R}_e^l, \ \boldsymbol{F}_{1,2} = \begin{bmatrix} 0 & f_u & -f_n \\ -f_u & 0 & f_e \\ f_n & -f_e & 0 \end{bmatrix}, \ \boldsymbol{F}_{2,1} = \begin{bmatrix} 0 & \frac{1}{R_M+h} & 0 \\ -\frac{1}{R_N+h} & 0 & 0 \\ -\frac{\tan\varphi}{R_N+h} & 0 & 0 \end{bmatrix}. \quad (6)$$

The system noise is denoted as $\boldsymbol{w}$ and assumed to be white with the covariance matrix

$$\mathbf{Q} = \begin{bmatrix} \sigma_f^2 \mathbf{I} & 0 \\ 0 & \sigma_\omega^2 \mathbf{I} \end{bmatrix}, \quad (7)$$

where σ_f and σ_ω are the variances of the measurement noise of the specific force and the angular rates. Equation 8 shows the corresponding observation model [15]:

$$\boldsymbol{z}_k = \boldsymbol{H}\delta\boldsymbol{x}_k + \boldsymbol{\eta}$$

$$\begin{bmatrix} 0 - v_{e,INS} \\ 0 - v_{n,INS} \\ 0 - v_{u,INS} \end{bmatrix}_k = \begin{bmatrix} 0 & 0 & 0 & 1 & 0 & 0 & 0 & 0 & 0 \\ 0 & 0 & 0 & 0 & 1 & 0 & 0 & 0 & 0 \\ 0 & 0 & 0 & 0 & 0 & 1 & 0 & 0 & 0 \end{bmatrix} \delta\mathbf{x}_k + \boldsymbol{\eta}, \quad (8)$$

where $\boldsymbol{\eta}$ refers to the observation noise. The observation noise is assumed to be normally distributed with zero-mean. The corresponding covariance matrix $\boldsymbol{R} = \sigma_v^2 \boldsymbol{I}$ contains the variances of the measurement noise σ_v.

To improve the performance of the proposed Zero-Velocity-Aided INS, prolonged standing is treated differently. Therefore, a modified stand-still mechanization is implemented according to [21]. This approach freezes the position as well as the heading under particular standstill conditions.

4.3. Zero-Velocity Detection

To detect zero-velocity events, the stance hypothesis optimal estimation (SHOE) detector [22, 1] it utilized (Formula 9). This zero-velocity detector is based on a fixed threshold and well suited for uniform motions. From the IMU output (accelerations $\boldsymbol{f}^b$, angular rates $\boldsymbol{\omega}_{ib}^b$) over a moving window of dimension N, the SHOE detector generates a test statistic T_k that decides if the pedestrian is moving or standing still. The test statistic is the average of the combination of the Euclidean norm of the acceleration data corrected by the (local) gravity term $\gamma\left(\varphi, h\right)$ and the Euclidean norm of the angular rates. The terms $\boldsymbol{f}_n^b \in \mathbb{R}^3$ and $\boldsymbol{\omega}_{ib_n}^b \in \mathbb{R}^3$ represent the single acceleration and angular rate vectors within the window. The acceleration and angular rate terms are weighed on basis of their signal quality ($\sigma_{f_{ZUPT}}$ and $\sigma_{\omega_{ZUPT}}$). The vector $\bar{\boldsymbol{f}}^b$ contains the mean values of each axis over N samples. The hypothesis that the IMU is stationary is accepted if T_k is below a pre-defined threshold α.

$$T_k = \begin{cases} 1, \ \text{if } \frac{1}{N}\sum_{n=k}^{k+N-1}\left(\frac{1}{\sigma_{f_{ZUPT}}^2}\left\|\boldsymbol{f}_n^b - \gamma\left(\varphi, h\right)\frac{\bar{\boldsymbol{f}}^b}{\|\bar{\boldsymbol{f}}^b\|}\right\|^2 + \frac{1}{\sigma_{\omega_{ZUPT}}^2}\left\|\boldsymbol{\omega}_{ib_n}^b\right\|^2\right) < \alpha \\ 0, \ \text{otherwise.} \end{cases} \quad (9)$$

4.4. Attitude Alignment

The initial sensor orientation can be determined when the system is stationary. The accelerometer measurements are used to compute the initial values for roll and pitch, which are then used to level the system [15]. The initialization of yaw is based on the magnetic heading [23]. Thus, the first 2 seconds of a stationary measurement phase from the accelerometer and magnetometer data is averaged and used for the computation of the initial attitude values. Roll and pitch are computed according to the Formulas 10 and 11 [15].

$$p_0 = \tan^{-1}\left(\frac{f_y}{\sqrt{f_x^2 + f_z^2}}\right) \tag{10}$$

$$r_0 = \tan^{-1}\left(\frac{-f_x}{f_z}\right) \tag{11}$$

The heading (yaw) is initialized using the magnetic heading. The magnetic heading y_m is computed using the normalized magnetic data $(\bar{m}_x, \bar{m}_y, \bar{m}_z)$ [23]:

$$y_{m_0} = \arctan\left(\frac{\bar{m}_x \cos r + \bar{m}_z \sin r}{\bar{m}_y \cos p + \bar{m}_x \sin r \sin p - \bar{m}_z \cos r \sin p}\right). \tag{12}$$

However, the magnetic heading y_m deviates from the true heading y. To improve the heading, the magnetic variation, which is currently about 4° 28' (positive to east) for Graz (Austria) [24], is taken into account.

5. Results

The results refer to the foot-mounted INS as a single system. Therefore, two areas in Graz (Austria) are chosen as test environments. The initial position is deviated from GNSS-data (if available) or manually set. The threshold for the zero-velocity detection was manually adapted for the different trails.

For the first test environment no reference data is available. In this area, three different tracks are recorded:

- **Track A:** Walking along a straight street ($\sim$ 1150 m)
- **Track B:** Walking ($\sim$ 750 m)
- **Track C:** Mixed-motions like slow/fast walking with forward/backward/lateral movements and jogging ($\sim$ 750 m)

Figure 4a shows Track A that goes along a straight road that is about 270 m long and 4.5 m wide. The test subject walks along the street 4 times ($<$ 1 km). As it can be seen, in the first 270 meters, the trajectories are approximately aligned with the path walked. Then the solutions start to drift away. The final horizontal positioning errors (comparison of start- and endpoint) after over 1 km are about 13 m and 45 m for the left and right trajectory, respectively. The vertical error is under 1 m in both cases (Figure 4b).
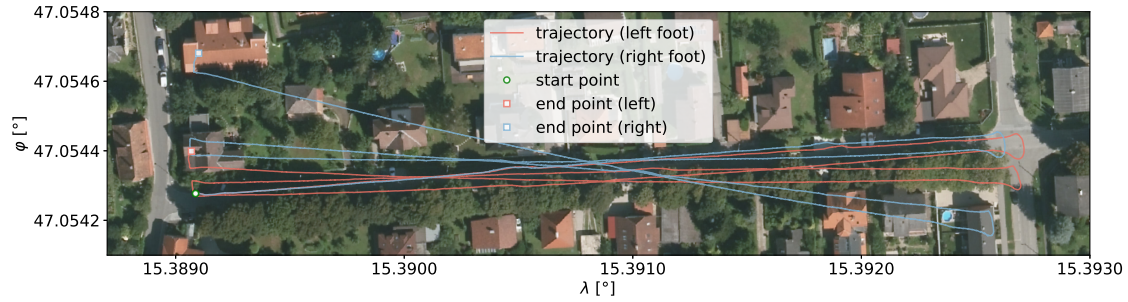
(a) INS trajectories.
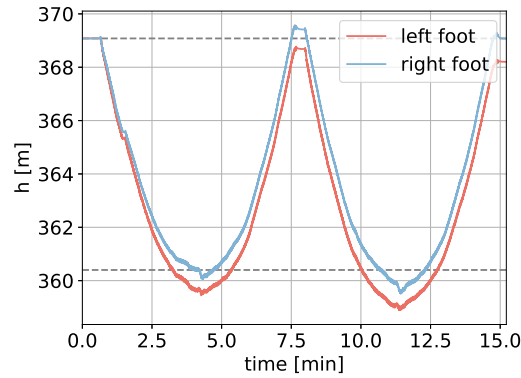
(b) Ellipsoidal height. Dotted lines: actual heights at both ends of the street.

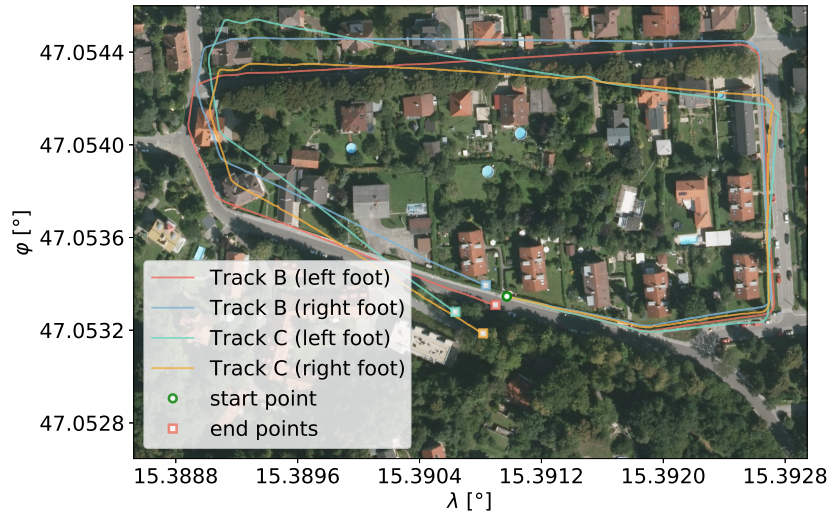**Figure 4:** Track A. Orthophoto RGB Status 2018 (©BEV – 2021).

Figure 5 pictures Tracks B and C. The first few meters show a satisfying positioning solution. The limitations are visible in Track C. Due to the use of a zero-velocity detector, which is based on a fixed threshold, irregular motions are not treated in the best way possible.

For the second test environment, a reference path with GNSS-based on real-time kinematic positioning (RTK) is generated. Therefore, the test subject carried a GNSS antenna during the recordings. The height component was corrected accordingly. For those tracks, another pair of sensors was used in comparison to the first measurement campaign. In total, three tracks are recorded:

- **Track D:** Walking forward
- **Track E:** Walking with forward/backward/lateral movements
- **Track F:** Walking forward combined with stair climbing

Figure 6 shows Track F as example. It pictures the INS trajectories as well as the ellipsoidal height over time. Between minute 5 and 6 the test subject goes down the steps, turns around, and goes back up. As time passes, the height drifts away. As it can be seen, the height component of the right foot performs better than the one of the left foot.

Table 1 lists the average root-mean-square error (ARMSE) of all tracks where reference data is available. The tests show reasonable results. In general, it is noticeable that the sensor of

Figure 5: INS trajectories of Track B and C. Orthophoto RGB Status 2018 (©BEV – 2021).

Table 1
Positioning error expressed in terms of average root-mean-square error (ARMSE). Comparison takes place step-wise only with RTK-fixed solutions.

Track	distance [m]	horizontal position error [m] left | right	vertical position error [m] left | right
D	~ 175	1.36 | 1.81	0.67 | 0.13
E	~ 185	1.60 | 1.70	0.89 | 0.10
F	~ 565	3.39 | 3.04	2.58 | 1.19

the right foot performs significantly better concerning the height estimation than the sensor mounted on the left foot.

The vertical accuracy in all tests is pretty good. Previous analysis, according to [25, 26], of inertial sensor errors based on Allan variance data showed that the gyroscope bias instability of the z-component is around 6 °/hr, whereas the bias instabilities of the x- and y-component vary from 8 °/hr to 12 °/hr. So, the gyroscope bias of the z-component shows a more stable behavior than the biases of the horizontal plane. The accelerometer biases do not differ significantly ($\approx$30 μg). Although the accelerometer and gyroscope biases result in an unbounded error growth of the vertical component [3], the drift seems comparatively moderate. However, since the internal sampling rate of XSens Dots is 800 Hz and is processed into a lower output rate of 60 Hz [14], it is difficult to give a detailed explanation.
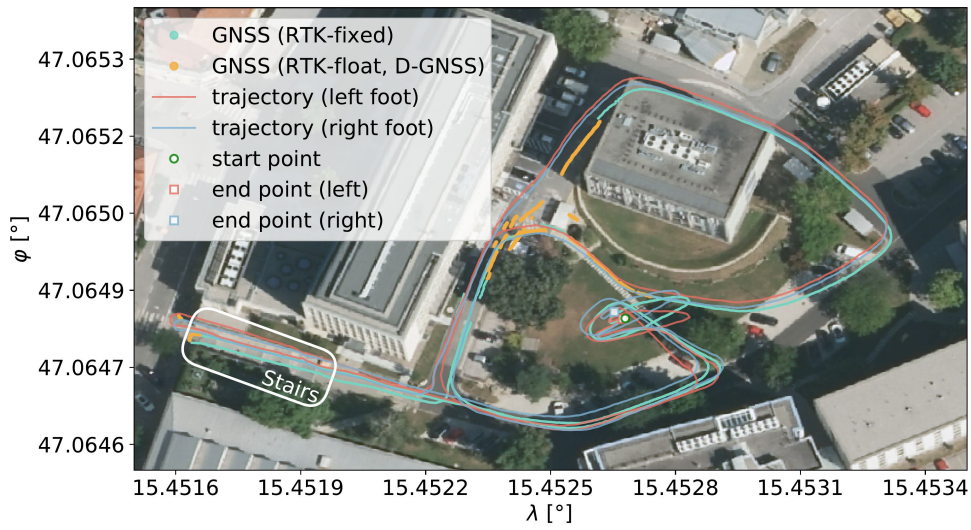
(a) INS trajectories.
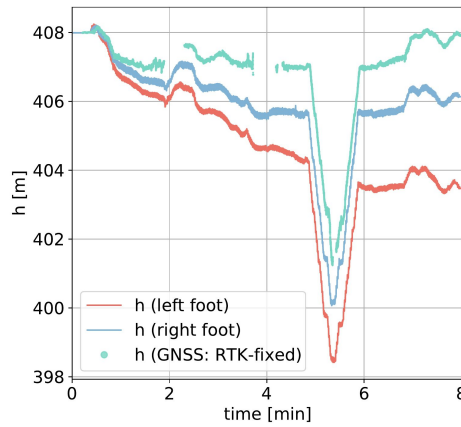
(b) Ellipsoidal height.

Figure 6: Track F: Walking combined with stair climbing ($\sim$ 565 m). Orthophoto RGB Status 2018 (©BEV – 2021).

6. Conclusion

The proposed navigation system relies on a dynamically built network of Wi-Fi RTT/UWB anchors. The coordinates of those anchors are derived from the INS and map solution. The position solutions from the foot-mounted INS as a single system reached satisfactory results over several hundred meters and that without any external support. Therefore, it should provide an accurate enough initial position estimate for the Wi-Fi/UWB access points.

The sensors showed different but manageable drift behaviors. A combined INS solution of the right and left leg could reduce the individual drifts. Studies [4, 12, 9] have shown that a

dual foot-mounted INS is an effective way to reduce systematic drift behavior. However, since the drift behavior varies between the different sensors, a dual-foot mounted INS could face limitations as discussed in [27].

The used zero-velocity detector (SHOE detector) is based on a fixed threshold approach. Thus, only uniform motion are treated well. Mixed motions, such as walking combined with running, are problematic. As shown in [1], zero-velocity detectors that are based on machine learning methodologies work well for varying motion types and outperform classical zero-velocity detectors. Future studies will focus on the improvement of zero-velocity detection so that all kinds of motion types are correctly processed.

The fusion of the foot-mounted INS with distance measurements and map information within a particle filter represents a promising approach to obtain a reliable navigation system for GNSS-denied environments.

Acknowledgments

References

[1] B. Wagstaff, V. Peretroukhin, J. Kelly, Robust Data-Driven Zero-Velocity Detection for Foot-Mounted Inertial Navigation, IEEE Sensors Journal 20 (2020) 957−967. URL: http://dx.doi.org/10.1109/JSEN.2019.2944412. doi:10.1109/jsen.2019.2944412.

[2] C. Fischer, H. Gellersen, Location and navigation support for emergency responders: A survey, IEEE Pervasive Computing 9 (2010) 38−47. doi:10.1109/MPRV.2009.91.

[3] B. Hofmann-Wellenhof, K. Legat, M. Wieser, Navigation, Springer Vienna, Vienna, 2003. doi:10.1007/978-3-7091-6078-7.

[4] G. Prateek, R. Girisha, K. Hari, P. Händel, Data Fusion of Dual Foot-Mounted INS to Reduce the systematic Heading Drift, in: 4th International Conference on Intelligent Systems, Modelling and Simulation, 2013, p. 208−213. doi:10.1109/ISMS.2013.46.

[5] J.-O. Nilsson, I. Skog, P. Händel, K. Hari, Foot-mounted ins for everybody - an open-source embedded implementation, in: Proceedings of the 2012 IEEE/ION Position, Location and Navigation Symposium, 2012, pp. 140−145. doi:10.1109/PLANS.2012.6236875.

[6] J.-O. Nilsson, I. Skog, P. Händel, A note on the limitations of ZUPTs and the implications on sensor error modeling, in: Proceeding of 2012-International Conference on Indoor Positioning and Indoor Navigation (IPIN), 13-15th November 2012, 2012. QC 20130116.

[7] J. Nilsson, D. Zachariah, I. Skog, P. Händel, Cooperative localization by dual foot-mounted

inertial sensors and inter-agent ranging, CoRR abs/1304.3663 (2013). URL: http://arxiv.org/abs/1304.3663. `arXiv:1304.3663`.

[8] S. Han, L. Wei, R. Li, W. Jingzhe, H. Yu, A Novel Cooperative Localization Method Based on IMU and UWB, Sensors 20 (2020) 467. doi:`10.3390/s20020467`.

[9] Y. Yang, R. Mu, J. Liang, Z. Xiao, B. Yan, S. Lin, G. Li, Accurate dual-foot micro-inertial navigation system with inter-agent ranging, in: 2016 Fourth International Conference on Ubiquitous Positioning, Indoor Navigation and Location Based Services (UPINLBS), 2016, pp. 152–161. doi:`10.1109/UPINLBS.2016.7809964`.

[10] M. Sun, Y. Wang, S. Xu, H. Qi, X. Hu, Indoor Positioning Tightly Coupled Wi-Fi FTM Ranging and PDR Based on the Extended Kalman Filter for Smartphones, IEEE Access 8 (2020) 49671–49684. doi:`10.1109/ACCESS.2020.2979186`.

[11] B. Krach, P. Robertson, Integration of foot-mounted inertial sensors into a bayesian location estimation framework, in: 2008 5th Workshop on Positioning, Navigation and Communication, 2008, pp. 55–61. doi:`10.1109/WPNC.2008.4510357`.

[12] I. Skog, J.-O. Nilsson, D. Zachariah, P. Händel, Fusing information from two navigation system using an upper bound on their maximum spatial separation, in: International Conference on Indoor Positioning and Indoor Navigation (IPIN), 2012, pp. 1–5. doi:`10.1109/IPIN.2012.6418862`.

[13] F. Uth, T. Hartmann, B. Späth, Real-time optimization of extraction and the logistic process in highly complex geological and selective mining settings, in: Horizon 2020 – the Framework Programme for Research and Innovation (2014-2020), 2017, p. 9–12.

[14] Xsens DOT User Manual, Document XD0502P, Revision D, XSens, 2020. https://www.xsens.com/xsens-dot.

[15] A. Noureldin, T. B. Karamat, J. Georgy, Fundamentals of inertial navigation, satellite positioning and their integration, Springer, Heidelberg, 2013.

[16] Koordinatensysteme, BEV – Bundesamt für Eich- und Vermessungswesen, 2006. https://www.bev.gv.at/pls/portal/docs/PAGE/BEV_PORTAL_CONTENT_ALLGEMEIN/0200_PRODUKTE/PDF/KOORD-SYS.PDF.

[17] T. Moder, C. Reitbauer, M. Dorn, M. Wieser, Calibration of smartphone sensor data usable for pedestrian dead reckoning, in: 2017 International Conference on Indoor Positioning and Indoor Navigation (IPIN), 2017, pp. 1–8. doi:`10.1109/IPIN.2017.8115910`.

[18] K. Legat, Untersuchungen zur GPS/INS-Integration, VGI – Österreichische Zeitschrift für Vermessung und Geoinformation 93 (2005) 72–82.

[19] R. M. Rogers, Applied Mathematics in Integrated Navigation Systems, Third Edition, American Institute of Aeronautics and Astronautics, Reston ,VA, 2007. doi:`10.2514/4.861598`.

[20] J. Wendel, Integrierte Navigationssysteme: Sensordatenfusion, GPS und Inertiale Navigation, 2011.

[21] J.-O. Nilsson, P. Händel, Standing still with inertial navigation, in: 2013 International Conference on Indoor Positioning and Indoor Navigation (IPIN), 2013.

[22] I. Skog, P. Händel, J.-O. Nilsson, J. Rantakokko, Zero-Velocity Detection—An Algorithm Evaluation, Biomedical Engineering, IEEE Transactions on 57 (2010) 2657 – 2666. doi:`10.1109/TBME.2010.2060723`.

[23] P. D. Groves, Principles of GNSS, inertial, and multi-sensor integrated navigation systems,

Technology and applications series, Artech House, Boston, 2008.

[24] Zentralanstalt für Meteorologie und Geodynamik (ZAMG), IGRF Deklinationsrechner, 2021. URL: https://www.zamg.ac.at/cms/de/geophysik/produkte-und-services-1/online-deklinationsrechner.

[25] J. Farrell, F. O. Silva, R. F., J. Wendel, IMU Error State Modeling for State Estimation and Sensor Calibration: A Tutorial, in: UC Riverside: Bourns College of Engineering, 2020. https://escholarship.org/uc/item/1vf7j52p.

[26] J. Jurado, C. M. Schubert Kabban, J. Raquet, A regression-based methodology to improve estimation of inertial sensor errors using Allan variance data, NAVIGATION 66 (2019) 251–263. URL: https://onlinelibrary.wiley.com/doi/abs/10.1002/navi.278. doi:https://doi.org/10.1002/navi.278. arXiv:https://onlinelibrary.wiley.com/doi/pdf/10.1002/navi.278.

[27] J. Lee, H. Ju, C. Park, Error Analysis of PDR System Using Dual Foot-mounted IMU, E3S Web of Conferences 94 (2019) 02007. doi:10.1051/e3sconf/20199402007.